Accepted Article

Original Article

Architecture of the Osteocyte Network Correlates with Bone Material Quality†

Michael Kerschnitzki[1,5,*], Philip Kollmannsberger[1,2,*], Manfred Burghammer[3], Georg N. Duda[4,5], Richard Weinkamer[1], Wolfgang Wagermaier[1], Peter Fratzl[1,5]

[1] Max Planck Institute of Colloids & Interfaces, Department of Biomaterials, D-14424 Potsdam, Germany
[2] ETH Zurich, Laboratory of Applied Mechanobiology, Department of Health Sciences and Technology, Wolfgang-Pauli-Str. 10, 8093 Zurich, Switzerland
[3] European Synchrotron Radiation Facility, 38043 Grenoble, France
[4] Charité, Julius Wolff Institute and Center for Musculoskeletal Surgery, Augustenburger Platz 1, D-13353 Berlin, Germany
[5] Berlin-Brandenburg School of Regenerative Therapies (BSRT), Augustenburger Platz 1, D-13353 Berlin, Germany

* These authors contributed equally to this work

Corresponding Author:
Peter Fratzl
Mail: fratzl@mpikg.mpg.de
Tel: 00493315679401
Max Planck Institute of Colloids & Interfaces
Department of Biomaterials
Am Mühlenberg 1
D-14424 Potsdam, Germany

Disclosures: All authors state that they have no conflicts of interest.

Keywords: Bovine/Ovine < ANIMAL MODELS, Collagen < MATRIX PROTEINS, Osteoblasts < OSTEOBLASTS and STEM CELLS, Bone mineralization < QUANTITATION

†This article has been accepted for publication and undergone full peer review but has not been through the copyediting, typesetting, pagination and proofreading process, which may lead to differences between this version and the Version of Record. Please cite this article as doi: [10.1002/jbmr.1927]

Additional Supporting Information may be found in the online version of this article.

Initial Date Submitted August 20, 2012; Date Revision Submitted February 19, 2013; Date Final Disposition Set March 6, 2013

Journal of Bone and Mineral Research
© 2013 American Society for Bone and Mineral Research
DOI 10.1002/jbmr.1927

Accepted Article

Abstract

In biological tissues such as bone, cell function and activity crucially depend on the physical properties of the extracellular matrix which the cells synthesize and condition. During bone formation and remodeling, osteoblasts get embedded into the matrix they deposit and differentiate to osteocytes. These cells form a dense network throughout the entire bone material. Osteocytes are known to orchestrate bone remodeling. However, the precise role of osteocytes during mineral homeostasis and their potential influence on bone material quality remains unclear. To understand the mutual influence of osteocytes and extracellular matrix, it is crucial to reveal their network organization in relation to the properties of their surrounding material. Here we visualize and topologically quantify the osteocyte network in mineralized bone sections with confocal laser scanning microscopy. At the same region of the sample, synchrotron small angle x-ray scattering is used to determine nanoscopic bone mineral particle size and arrangement relative to the cell network. Major findings are that most of the mineral particles reside within less than a micrometer from the nearest cell network channel and that mineral particle characteristics depend on the distance from the cell network. The architecture of the network reveals optimization with respect to transport costs between cells and to blood vessels. In conclusion, these findings quantitatively show that the osteocyte network provides access to a huge mineral reservoir in bone due to its dense organization. The observed correlation between the architecture of osteocyte networks and bone material properties supports the hypothesis that osteocytes interact with their mineralized vicinity and thus, participate in bone mineral homeostasis.

Accepted Article

Introduction

Biological tissues are characterized by interactions between cells and their environment. This environment is usually extracellular matrix formed and controlled by the cells. A particularly interesting case of the interplay between cells and surrounding extracellular matrix are osteocytes in bone. Osteocytes are the most abundant bone cell (1). They derive from bone-forming osteoblasts which get embedded in the material they synthesize (2). During the deposition of unmineralized bone matrix, which subsequently mineralizes, osteocytes form dendritic cell processes, thereby establishing connections with their neighboring cells and the bone surface (3). After the tissue has mineralized, these processes reside within a dense network of lacunar and canalicular cavities (4). Osteocytes are multifunctional and are known to orchestrate the complex interplay of bone resorption and formation by osteoclasts and osteoblasts on the bone surface (5-8) by translating mechanical strains into biochemical signals (9). For this mechanotransductive function, the intricate network between the cells seems of decisive importance. Moreover, osteocytes are considered to play an active role in mineral homeostasis by directly interacting with their mineralized vicinity (1,10). Here again, the dense network of lacunar and canalicular spaces is crucial as it provides abundant bone surfaces exposed to the cells. This surface area is estimated to be more than 100 fold larger than the area available to osteoblasts and osteoclasts (11).

Consequently, it is conceivable that interactions between osteocytes and the enormous bone surface they are facing could significantly contribute to mineral homeostasis, thus maintaining circulating ion levels in the body during events of severe ion demands (11). In recent years, evidence has accumulated that osteocytes are involved in controlling body phosphate levels (12) and might be capable of resorbing their pericellular bone mineral (13,14). However, the proposed interactions of the cells with their surrounding material should leave traces of their activity in the mineralized matrix. Therefore, a promising approach to better understand the relationship between osteocytes and their surrounding mineralized matrix is to spatially correlate the osteocyte network architecture

with bone material properties describing bone quality (15) in the proximity and far away from the cell network.

To date, this approach was hardly followed because it requires a combination of imaging methods with high spatial resolution. A suitable methodology at the crossover between biology and material science has to provide at once, detailed information on the three-dimensional structure of osteocyte lacunar-canalicular systems (OLCS) (16) and on the mineral properties of the adjacent bone material, both with at least a micrometer resolution. To tackle this, we developed a new method allowing a precise quantitative correlation between the cell network and the surrounding bone material. We used confocal laser scanning microscopy combined with rhodamine staining (17) to visualize and quantify the OLCS in undemineralized bone sections (Figure 1). Complementary, synchrotron radiation in a micro focus setting was employed to scan the very same pre-characterized bone samples to measure the small angle x-ray scattering (SAXS) signal with a submicrometer resolution. With the mineral particles having a thickness of only a few nanometers, SAXS is the appropriate method to determine nanoscopic material properties such as the mineral particle arrangement (ρ) and thickness (T) parameters in a position resolved way (18). These parameters describe bone mineralization and organization, both closely associated to bone material quality (19).

With this approach, we succeeded to measure a direct correlation between the osteocyte network architecture and bone material quality. In this work, we show in particular a detailed three-dimensional visualization of the osteocyte network in bone, which allows us to **(i)** characterize cell-cell connectivity via complex canalicular structures. These data not only reveal present network logistics, but also allows **(ii)** determining average distances between the cell network and the mineralized bone matrix. Finally, these distance data are **(iii)** correlated to the bone material quality

Accepted Article

elucidated by SAXS measurements to better understand the relationship between osteocyte network architecture and bone mineral embedded in their proximity inside the extracellular matrix.

Materials and Methods

Bone samples and sample preparation

Native ovine fibrolamellar (plexiform) bone samples, not yet showing secondary osteons due to remodelling, were collected from the midshaft region of the femur of a mature 5 year old sheep. For initial preparation, samples were anhydrously cut with a low speed diamond saw (IsoMet, Buehler GmbH, Duesseldorf, Germany). The resulting plates with a cross section of 5 × 5 mm and an initial thickness of 200 µm were further polished to a final thickness of 20 µm using an automatic polisher (Logitech PM5, Logitech Ltd. Glasgow, UK). During all steps of sample preparation, ethylene glycol was used as an anhydrous sample preparation medium. After polishing, samples were washed in pure ethanol to remove remaining ethylene glycol. Bone samples were examined to identify regions of interest (ROI's) and subsequently marked by creating artificial notches with laser micro dissection (PALM MicroBeam C, P.A.L.M. Microlaser Technologies GmbH, Bernried, Germany). Tagging the identified ROI's allows precise matching of data.

Confocal laser scanning microscopy

Bone samples were stained over night with rhodamine-6G (Sigma Aldrich GmbH, Germany) which was dissolved (0.002 % wt) in methyl metacrylate (MMA) solution. As described elsewhere (20), the fast diffusion of rhodamine through the bone samples leads to a fluorescent labeling of all internal surfaces such as those from blood vessels, osteocyte lacunae and canaliculi. After washing with pure ethanol for three times, confocal z-stacks of the previously identified ROI's were acquired using a Leica DM IRBE (Leica Mikroskopie und Systeme GmbH, Germany) equipped with a 100× oil immersion microscope objective with a numerical aperture of 1.4. The resulting images have a diffraction-limited resolution of about 250-300 nm. The average spacing of

Accepted Article

structures in the lacuno-canalicular network was found to be on the order of 2 µm using FIB-SEM (21) and much smaller distances are likely to occur only around junctions, therefore the analysis of the network structure is not compromised by the resolution limit.

Thresholding and segmentation of image data

The original data were Gaussian filtered (5x5x5 kernel, sd=0.65) before automatic thresholding was applied to convert the intensity stack into a binary volume with foreground (lacuno-canalicular network) and background (bone matrix) voxels (figure 1). The threshold was determined by fitting a double exponential to the stack histogram, corresponding to image data and noise, respectively, and setting the threshold to the intensity value at which the noise contribution fell below 1%. Since the analysis is robust to the choice of the threshold within a certain range (see supplementary figure 1), other thresholding algorithms described in literature will also work, depending on the level of noise in the images. Discretisation noise was removed by morphological closing (dilation followed by erosion using a 3x3x3 kernel). The binary volume was further cleaned by discarding small isolated foreground clusters and by converting isolated background components (voids) to foreground.

In the next step, larger structures (cell lacunae or blood vessels) were automatically separated from the canalicular network. First, the distance transform of the foreground was calculated, assigning to every foreground voxel its Euclidean distance to the nearest background voxel. Subsequently, all connected regions with a distance of at least 1 µm from the background and a size of at least 16 µm³ were defined as cells or blood vessels. Finally, the identified cells and blood vessels were expanded (dilation with a 3x3x3 kernel) until reaching a distance of 0.6 µm to the background to approximate the original cell shape. The choice of all parameter values was validated on a number of image stacks and then kept constant throughout the analysis of all data.

Accepted Article

Accepted Article

Medial axis skeletonization and network analysis

The structure of the cell network was derived from the binarized images by computing the medial axis of the foreground. Voxels were iteratively removed from the surface of the volume if removing them did not change the connectivity of their 26-neighborhood and if they had more than one neighbour in their 26-neighbourhood (otherwise they are endpoints). We implemented the homotopic thinning algorithm described by Lee et al (22), using parallel rechecking in 8 subvolumes with non-overlapping neighbourhoods. The result was a one voxel thick medial axis skeleton that is homotopic to the original image (figure 1c).

In the next step, the voxel skeleton was converted into a network topology described by nodes, links and cells. Clusters of voxels with more than two neighbours each were defined as node, and groups of connected voxels with two neighbours each were defined as links or branches (if connected to one node only). All branches shorter than 1 μm and all loops and isolated nodes were removed (figure 1d, e).

This topology was used to calculate length and degree distributions of the network, and to assign the distance to the nearest cell through the network to every voxel in a link. A link matrix (dimension N × N, where N = number of nodes) was calculated, with entries a_{ij} denoting the distance between node i and node j if there was a direct link between the two. From this matrix, the shortest path between two nodes within the network was determined using Dijkstra's algorithm.

Finally, the logical structure was converted back into a cleaned voxel skeleton, which was used for analyzing the distance of the bone matrix from the cell network. For this purpose, the distance transform of the bone matrix to the cell network was calculated, assigning to each matrix voxel its

Euclidean distance to the nearest voxel in a cell, and to the nearest voxel in the lacuno-canalicular network including cells.

All image analysis and quantification algorithms were implemented in MATLAB R2009a (The MathWorks, USA) using the image processing toolbox and the MatlabBGL graph library. The MATLAB code is available from the authors on request.

Small angle x-ray scattering (SAXS) measurements

Bone samples were scanned at the Nanofocus beamline ID13 at the European Synchrotron Radiation Facility (ESRF), Grenoble, France using a monochromatic 14 keV x-ray beam ($\lambda = 0.886$ Å) with a beam size of 500 nm. An ESRF FReLoN detector with 2048 × 2048 pixels and a corresponding pixel size of 51.5 × 50.7 µm² was used to record the scattering patterns. Bone sections were stabilized with a lead frame and screwed on a sample holder which was magnetically mounted to the sample stage. During scanning, the stage was translated perpendicularly to the beam with a step size of 1 µm. Typical scan areas had a dimension of 200 × 200 µm, including around 40.000 recorded SAXS patterns.

Data correction

The accurate sample to detector distance and beam centre position were determined from the diffraction patterns of hydroxyapatite (HAP) standard powder using Fit2d (23) software. Scattering intensity data were corrected in relation to empty beam (EB) intensities following the equation $I_{corrected} = \frac{I_{sample}}{t} - I_{EB}$ with t as the correction factor defined as $t = t_1 * t_2 = \left(\frac{I_{sample,diode}}{I_{EB,diode}}\right) \cdot \left(\frac{Monitor_{sample,mar}}{Monitor_{EB,mar}}\right)$. Here, t_1 is the correction of the transmission intensity (measured with a beam diode) which is the ratio of the Intensity at the Sample (I_{sample}) and the empty beam intensity (I_{EB}) and t_2 as the correction of the decreasing x-ray beam intensity during

Accepted Article

scanning, measured with a beam monitor. For t_1 the decrease of the ring current during the transmission scan was neglected since transmission scans were very short.

Data analysis

Scattering data were analyzed using Autofit (custom made analysis software, C. Li, Max Planck Institute of Colloids and Interfaces, Potsdam, Germany). For calculation of the average mineral particle orientation in the exposed sample volume, the scattering intensity was integrated over q as a function of the azimuthal angle χ. The distribution of the integrated intensity along q over χ describes the average direction (peak position of both intensity maxima) and the fraction of aligned mineral particles in the exposed sample volume, described by the rho parameter which corresponds to $Rho = \frac{A_1 + A_2}{A_1 + A_2 + A_0} = \frac{particles_{aligned}}{particles_{all}}$. The amount of aligned particles is represented by $A_1 + A_2$. The baseline area A_0 represents the amount of unaligned mineral particles residing within the exposed sample volume (supplementary figure 2). The alignment of mineral particles corresponds to the orientation of the collagen matrix as the collagen molecules are directing mineral particle growth (19).

For calculation of the mineral particle thickness parameter (T parameter), the decay of the scattering intensity integrated over all χ at larger q-values was analyzed. The T-parameter is defined as $T = \frac{4\phi(1-\phi)}{\sigma} = \frac{4}{\pi} \cdot \frac{\bar{I}}{P}$ (24), with ϕ as the volume fraction of the mineral phase, σ as the surface area of mineral particles per unit volume, P as the Porod constant (intercept of the Porod fit) determined from the Porod plot and $\bar{I}$ as the integration of the Kratky plot (supplementary figure 3), defined as

$$\bar{I} = \int_0^\infty q^2 I(\vec{q}) dq = \int_0^{q,Kratky,\min} q^2 I(\vec{q}) dq + \int_{q,Kratky.\min}^{q,Porod,\min} q^2 I(\vec{q}) dq + \int_{q,Porod,\min}^\infty q^2 I(\vec{q}) dq$$ which further simplifies to

$$\bar{I} = \frac{1}{2} I_{Kratky,\min} \cdot q_{Kratky.\min} + \int_{q,Kratky,\min}^{q,Porod,\min} q^2 I(\vec{q}) dq + \frac{P}{q_{Porod,\min}}$$ as for biphasic systems $I(q) \xrightarrow{q \to \infty} \frac{P}{q^4}$.

Accepted Article

Fitting parameters for the Porod plot were set to $Porod_{min}$ = 1.5 and $Porod_{max}$ = 2.8 nm^{-1}. The fit parameter $Kratky_{min}$, from which the Kratky plot is interpolated for small q-values (due to insufficient q-resolution), was set to 0.3 nm^{-1}.

Results

Extensive osteocyte interconnectivity via canalicular structures

The graph representation of the canalicular network allows firstly the analysis of potential cell-cell connectivity via the canalicular structures (Figure 2). Our analysis showed a strong interconnection between cells (Figure 2a) but surprisingly, this interconnection extends not only to the neighboring cell lacunae, but to all lacunae within the analyzed bone volume (Figure 2b). In addition, all cell lacunae have direct access to their neighboring blood vessels via the network, which is crucial for nutritional supply (Figure 2a, b). To quantify average transport lengths along canalicular structures towards the cells, we estimated the network region controlled by each cell by assigning the nearest cell to each network voxel (Figure 2c). The distribution of the shortest distance of a network voxel to its adjacent cell shows that almost 70 % of the canalicular network is within a transport distance of only 10 µm (Figure 2e).

Secondly, we quantified topological parameters of the network, which are of importance for its function as a communication network and yield information on the physical constraints present during its formation (25). The edge lengths l in the network follow an exponential distribution $p(l) \sim exp(-\alpha l)$ with a slope α = 0.7 μm^{-1}, the mean canalicular length (travel distance) between the nodes is about 2.15 µm (Figure 2g). The degree d of nodes (i.e., the number of edges, respectively canaliculi, that connect to it) is also exponentially distributed, $p(d) \sim exp(-\beta d)$ with a slope β = 0.87, the mean degree is 3.25 (Figure 2f). The large amount of branching nodes (with degree 3) shows the mainly dendritic nature of the canalicular network. However, 35% of nodes show a rather

Accepted Article

interwoven type, as 4 up to more than 10 individual canaliculi connect to these junctions (Figure 2d).

Majority of mineral resides within a micrometer from the cell network

The processed osteocyte network data also contain quantitative information about the amount of mineral residing in the vicinity of the osteocyte network (Figure 3). For this quantification, the Euclidian distance of every matrix voxel to the closest cell (Figure 3a) was calculated. Distance distributions show that 80 % of all matrix voxels reside below a distance of 10 μm to the adjacent cell (Figure 3b). However, the distance distribution changes dramatically by considering not only the cell lacunae, but the entire network including the canaliculi (Figure 3b). We found that within a distance as small as 1 micrometer, already 60 % and within 1.4 μm, 80 % of the mineralized matrix are located (Figure 3d).

Bone material quality depends on network architecture

Position resolved nanoscopic mineral properties such as the mineral particle thickness parameter (T) and orientation (ρ) describing bone material quality (see Materials and Methods) were measured in a micro-focus setting by scanning small angle x-ray scattering (SAXS) in pre-characterized bone sections featuring distinct osteocyte network organizations (Figure 4). The mineral particle thickness (Figure 4b) and particle orientation (Figure 4c) are increased in areas of dense, highly aligned osteocyte network showing values of $T > 2.5$ nm and $\rho > 0.5$, respectively. Within bone regions that exhibit loose, unorganized network structures, mineral particles are thinner ($T < 2.5$ nm) and poorly oriented ($\rho < 0.5$). The direction of mineral particle alignment is always parallel to the osteocyte long axis, respectively perpendicular to the direction of the canalicular alignment. Moreover, in the direct vicinity of osteocyte lacunae within regions of a highly organized network, lower mineral particle thicknesses T and orientations ρ are apparent (Figure 4d).

Accepted Article

Accepted Article

The correlation between the nanoscopic material properties and the position of material in relation to the network is shown in Figure 5 using the example of the mineral particle thickness parameter T. Large values of T are only obtained close to the osteocyte network. The distribution displays a sharp peak of the particle thickness at T = 2.75 nm with a standard deviation of 0.1 nm. This bone material is located in regions with a dense, organized osteocyte network. For low values of the T parameter, the correlation between T and the distance to the network is much weaker. This occurs in regions with a loose, unorganized osteocyte network. The separation between the two different ways of organization of the osteocyte network is reflected in the bimodal distribution of the mineral particle thickness T. In other words, dense osteocyte networks feature highly oriented bone mineral with homogeneously thick mineral particles, whereas in areas of loose osteocyte networks, bone material is less organized and thus, bone material quality rather low (19,24).

Discussion:

Our combined approach of visualizing and quantifying confocal laser scanning microscopy (CLSM) data together with position resolved SAXS mapping reveal the complex three-dimensional structure of osteocyte networks in mineralized bone tissue in correlation with the distribution of nanoscopic mineral properties. This allows the detection and further analysis of nanoscopic network structures and even the application of theoretical network analysis. This reveals not only extensive osteocyte connectivity, but also typical canalicular network properties such as node point characteristics and mean travel lengths through the network.

Our data show that all osteocytes in the visualized volume – and not only neighboring cells – are interconnected via the extracellular spaces of the canalicular network. This mainly dendritic canalicular network exhibits a strongly interwoven characteristic with a high abundance of connecting canaliculi in the vicinity of osteocytes and within osteocytic layers. The exponential decay of the canalicular node degree distribution reveals the single-scale character of the

Accepted Article

canalicular network. Single-scale networks are characterized by the fact that physical constraints such as transport costs influence the addition of new links (25). In bone this may indicate an optimization of the channel network with respect to transport costs of nutrients and signals. Thus, these dense and multi-connected canalicular structures create an efficient communication network also being robust against local interruptions due to microcracking for example, which can be a consequence of severe mechanical loading (26). However, it needs to be kept in mind that our network data describe the complex system of extracellular voids (that is the "highway-system") but not the cells themselves (which would be responsible for the actual "traffic"). Thus, these findings lead to intriguing considerations concerning the flexibility of cellular connections residing within the canalicular structures, as live-imaging experiments suggest that osteocytes permanently expand and contract their dendrites inside these voids in response to stimuli (27). This could be of high importance as stimulated formation of temporarily connected dendrites could strongly modify cell network characteristics such as the clustering of or the path length between cells. In network theory these two network parameters are used to classify networks to regular, random or small-world networks (28).

The complex organization of the osteocyte network not only seems to be optimized for efficient communication between the cells[0], but it has the potential to provide access to most of the mineralized bone matrix due to its dense architecture. In highly organized (dense) regions of the osteocyte network, these structures are arranged to feature short distances to the mineral. Indeed, calculations of average cell network-mineral distances show that the majority of bone mineral resides within a distance of only 1 µm to the nearest cell network structure. This leads to a reduction by almost one order of magnitude of the distance that mineral has to diffuse through the bone material before reaching the canalicular network, in which even large molecules can diffuse relatively fast (29), instead of reaching a cell lacuna. This becomes even more significant when keeping in mind that diffusion times usually scale with the square of the covered distance. Scanning

Accepted Article

SAXS investigations of nanoscopic bone mineral properties on the same sample sections show a strong correlation between mineral characteristics and the osteocyte network structures. We find that highly organized bone mineral featuring relatively thick and highly oriented particles – associated to high bone material quality – predominantly resides at short distances to the next cell or canalicular structure. In contrast, mineral particles at larger distances from the network are less organized and show broader distributions in thickness and orientation. These findings support the hypothesis that osteocytes directly control bone mineral in their vicinity (1,10), but also that a dense and well-organized osteocyte network may be crucial to facilitate this control by either active (cellular) or passive (dissolution/apposition) mechanisms, thereby leading to higher bone material quality.

How cells are influenced by their material environment, such as stiffness (30) or substrate geometry (31) and reciprocally, how these cells manipulate their environment, is not only of paramount importance in the context of the biological function of cells. An understanding of this bidirectional feedback mechanism between cells and the surrounding material can fundamentally change the future design of in vitro experiments using cell cultures. We believe that the utilization of our approach to combine experimental techniques from biology and materials science will provide important new insights for this interplay. It allows, in the very same biological specimen, to reveal both, the organization of the cells together with the impact of cellular action on the material properties of the surrounding extracellular matrix.

The samples used in this study were from primary fibrolamellar (plexiform) bone. However, our findings can be generalized to other types of lamellar bone since the degree of organization of the osteocyte network is similar in different types of lamellar bone of different species, but differs significantly from that found in woven bone (17). In previous work, we found that osteocyte networks qualitatively mirror bone formation which in the case of lamellar bone is a layer-by-layer

process (17,20). Our method for network quantification presented here could therefore be used in the future to study the role of cellular network organization for the formation of lamellar or woven bone, or to relate pathological changes on bone material properties to the characteristics of the osteocyte network structure.

In conclusion, osteocytes form dense and highly organized networks throughout the mineralized matrix, with the majority of bone mineral residing just within a distance of one micron from it. The degree of organization of the network indicate a high level of communication between cells, which is rather reminiscent of a neuronal network (32) and was just hidden by the all too visible mineralized matrix. Many comparable studies have been carried out on complex brain networks. These described a modification of network characteristics, such as clustering and mean path length, due to cognitive and psychiatric disturbances present in patients with Alzheimer's disease or schizophrenia (33). Concerning the osteocyte network architecture in bone, in principle it is also conceivable to relate a modification of these network parameters to bone diseases such as osteoporosis. In this regard, disturbances in the osteocyte network organization have a strong impact on fluid flow, diffusion of ions, hormones and signaling molecules, all factors promoting cellular communication and mechanosensation via the osteocyte lacunar canalicular network (34-36).and thus, ultimately affecting bone material quality (15).

Accepted Article

Accepted Article

Acknowledgements

We thank A. M. Martins and B. Schonert from the Max Planck Institute of Colloids and Interfaces for technical assistance and H. Schell from the Julius Wolff Institute for providing ovine bone samples collected in the SFB 760. M.K. is funded by Bundesministerium für Bildung und Forschung (BMBF, grant-number: 01 EC 1006C, project 9133). Author's roles: Study design: RW, WW, and PF. Study conduct: MK, PK, MB, GD and WW. Data Collection: MK, PK, MB, and WW. Data Analysis: MK, PK, and WW. Data Interpretation: MK, PK, MB, GD, RW, WW, and PF. Writing the Manuscript: MK, PK, GD, RW, WW, and PF. WW takes responsibility for the integrity of the data analysis.

Accepted Article

References

1. Bonewald LF 2011 The Amazing Osteocyte. Journal of Bone and Mineral Research **26**(2)**:**229-238.
2. Barragan-Adjemian C, Nicolella D, Dusevich V, Dallas MR, Eick JD, Bonewald LF 2006 Mechanism by which MLO-A5 late osteoblasts/early osteocytes mineralize in culture: Similarities with mineralization of lamellar bone. Calcified Tissue International **79**(5)**:**340-353.
3. Lanyon LE, Rubin, Raisz, Marotti, Lees 1993 OSTEOCYTES, STRAIN DETECTION, BONE MODELING AND REMODELING. Calcified Tissue International **53:**S102-S107.
4. Franz-Odendaal TA, Hall BK, Witten PE 2006 Buried alive: How osteoblasts become osteocytes. Developmental Dynamics **235**(1)**:**176-190.
5. Huiskes R, Ruimerman R, van Lenthe GH, Janssen JD 2000 Effects of mechanical forces on maintenance and adaptation of form in trabecular bone. Nature **405**(6787)**:**704-706.
6. Nakashima T, Hayashi M, Fukunaga T, Kurata K, Oh-Hora M, Feng JQ, Bonewald LF, Kodama T, Wutz A, Wagner EF, Penninger JM, Takayanagi H 2011 Evidence for osteocyte regulation of bone homeostasis through RANKL expression. Nature Medicine **17**(10)**:**1231-1234.
7. Tatsumi S, Ishii K, Amizuka N, Li MQ, Kobayashi T, Kohno K, Ito M, Takeshita S, Ikeda K 2007 Targeted ablation of Osteocytes induces osteoporosis with defective mechanotransduction. Cell Metabolism **5**(6)**:**464-475.
8. Poole KES, van Bezooijen RL, Loveridge N, Hamersma H, Papapoulos SE, Lowik CW, Reeve J 2005 Sclerostin is a delayed secreted product of osteocytes that inhibits bone formation. Faseb Journal **19**(10)**:**1842-+.
9. Kleinnulend J, Vanderplas A, Semeins CM, Ajubi NE, Frangos JA, Nijweide PJ, Burger EH 1995 SENSITIVITY OF OSTEOCYTES TO BIOMECHANICAL STRESS IN-VITRO. Faseb Journal **9**(5)**:**441-445.
10. Teti A, Zallone A 2009 Do osteocytes contribute to bone mineral homeostasis? Osteocytic osteolysis revisited. Bone **44**(1)**:**11-16.
11. Aarden EM, Burger EH, Nijweide PJ 1994 FUNCTION OF OSTEOCYTES IN BONE. Journal of Cellular Biochemistry **55**(3)**:**287-299.
12. Feng JQ, Ward LM, Liu SG, Lu YB, Xie YX, Yuan BZ, Yu XJ, Rauch F, Davis SI, Zhang SB, Rios H, Drezner MK, Quarles LD, Bonewald LF, White KE 2006 Loss of DMP1 causes rickets and osteomalacia and identifies a role for osteocytes in mineral metabolism. Nature Genetics **38**(11)**:**1310-1315.
13. Tazawa K, Hoshi K, Kawamoto S, Tanaka M, Ejiri S, Ozawa H 2004 Osteocytic osteolysis observed in rats to which parathyroid hormone was continuously administered. Journal of Bone and Mineral Metabolism **22**(6)**:**524-529.
14. Qing H, Ardeshirpour L, Pajevic PD, Dusevich V, Jähn K, Kato S, Wysolmerski J, Bonewald LF 2012 Demonstration of osteocytic perilacunar/canalicular remodeling in mice during lactation. Journal of Bone and Mineral Research**:**n/a-n/a.
15. Seeman E, Delmas PD 2006 Mechanisms of disease - Bone quality - The material and structural basis of bone strength and fragility. New England Journal of Medicine **354**(21)**:**2250-2261.
16. Schneider P, Meier M, Wepf R, Muller R 2010 Towards quantitative 3D imaging of the osteocyte lacuno-canalicular network. Bone **47**(5)**:**848-858.
17. Kerschnitzki M, Wagermaier W, Roschger P, Seto J, Shahar R, Duda GN, Mundlos S, Fratzl P 2011 The organization of the osteocyte network mirrors the extracellular matrix orientation in bone. Journal of Structural Biology **173**(2)**:**303-311.
18. Rinnerthaler S, Roschger P, Jakob HF, Nader A, Klaushofer K, Fratzl P 1999 Scanning small angle X-ray scattering analysis of human bone sections. Calcified Tissue International **64**(5)**:**422-429.

19. Fratzl P, Gupta HS, Paschalis EP, Roschger P 2004 Structure and mechanical quality of the collagen-mineral nano-composite in bone. Journal of Materials Chemistry **14**(14)**:**2115-2123.
20. Kerschnitzki M, Wagermaier W, Liu YF, Roschger P, Duda GN, Fratzl P 2011 Poorly Ordered Bone as an Endogenous Scaffold for the Deposition of Highly Oriented Lamellar Tissue in Rapidly Growing Ovine Bone. Cells Tissues Organs **194**(2-4)**:**119-123.
21. Schneider P, Meier M, Wepf R, Muller R 2011 Serial FIB/SEM imaging for quantitative 3D assessment of the osteocyte lacuno-canalicular network. Bone **49**(2)**:**304-311.
22. Lee TC, Kashyap RL, Chu CN 1994 BUILDING SKELETON MODELS VIA 3-D MEDIAL SURFACE AXIS THINNING ALGORITHMS. Cvgip-Graphical Models and Image Processing **56**(6)**:**462-478.
23. Hammersley AP, Svensson SO, Hanfland M, Fitch AN, Hausermann D 1996 Two-dimensional detector software: From real detector to idealised image or two-theta scan. High Pressure Research **14**(4-6)**:**235-248.
24. Fratzl P, Fratzlzelman N, Klaushofer K, Vogl G, Koller K 1991 NUCLEATION AND GROWTH OF MINERAL CRYSTALS IN BONE STUDIED BY SMALL-ANGLE X-RAY-SCATTERING. Calcified Tissue International **48**(6)**:**407-413.
25. Amaral LAN, Scala A, Barthelemy M, Stanley HE 2000 Classes of small-world networks. Proceedings of the National Academy of Sciences of the United States of America **97**(21)**:**11149-11152.
26. Nalla RK, Kinney JH, Ritchie RO 2003 Mechanistic fracture criteria for the failure of human cortical bone. Nature Materials **2**(3)**:**164-168.
27. Veno PA, Nicolella DP, Sivakumar P, Kalajzic I, Rowe DW, Bonewald LF, Harris SE, Dallas SL 2006 Live imaging of osteocytes within their lacunae reveals cell body and dendrite motions. Journal of Bone and Mineral Research **21:**S38-S39.
28. Watts DJ, Strogatz SH 1998 Collective dynamics of 'small-world' networks. Nature **393**(6684)**:**440-442.
29. Wang LY, Wang YL, Han YF, Henderson SC, Majeska RJ, Weinbaum S, Schaffler MB 2005 In situ measurement of solute transport in the bone lacunar-canalicular system. Proceedings of the National Academy of Sciences of the United States of America **102**(33)**:**11911-11916.
30. Discher DE, Janmey P, Wang YL 2005 Tissue cells feel and respond to the stiffness of their substrate. Science **310**(5751)**:**1139-1143.
31. Kollmannsberger P, Bidan CM, Dunlop JWC, Fratzl P 2011 The physics of tissue patterning and extracellular matrix organisation: how cells join forces. Soft Matter **7**(20)**:**9549-9560.
32. Turner CH, Robling AG, Duncan RL, Burr DB 2002 Do bone cells behave like a neuronal network? Calcified Tissue International **70**(6)**:**435-442.
33. Bullmore E, Sporns O 2009 Complex brain networks: graph theoretical analysis of structural and functional systems. Nature Reviews Neuroscience **10**(3)**:**186-198.
34. Bonewald LF, Johnson ML 2008 Osteocytes, mechanosensing and Wnt signaling. Bone **42**(4)**:**606-615.
35. Robling AG, Castillo AB, Turner CH 2006 Biomechanical and molecular regulation of bone remodeling Annual Review of Biomedical Engineering, vol. 8. Annual Reviews, Palo Alto, pp 455-498.
36. Xiong JH, O'Brien CA 2012 Osteocyte RANKL: New insights into the control of bone remodeling. Journal of Bone and Mineral Research **27**(3)**:**499-505.

Accepted Article

Accepted Article

Figure legends

Figure 1: Osteocyte network visualization and quantification. (a) Bone samples are stained with rhodamine which diffuses through all microscopic and nanoscopic extracellular spaces representing the osteocyte network. The location of the dye is measured with confocal laser scanning microscopy. (b) z-projection of a confocal image stack. (c) Segmentation of the data into mineralized matrix (black), microscopic bone features such as blood vessels and osteocyte lacunae (shades of blue) and the medial axis skeleton of the canalicular network (shades of red). (d) subvolume showing confocal raw data (grey), segmented osteocyte lacunae (blue) and skeletonized canalicular structures (shades of red depicting the z-value of each canalicular voxel) (e) Conversion of osteocyte network data to a graph structure consisting of cell lacunae (blue), canalicular nodes (yellow dots) and edges (black lines). Edges represent connections between nodes of the canalicular network. (f) Combination of raw image and processed network data from (d) and (e) with segmented cell lacunae (blue) and skeletonized canalicular network (shades of red) in a representative subvolume of 25 x 40 x 4 µm. Scale bars are 20 µm.

Figure 2: Cell-cell interconnectivity and canalicular network analysis. (a) Yellow lines depict direct connections between individual segmented cells (blue) via the canalicular network structures. (b) Exemplarily for one cell, the shortest direct connection through the canalicular system to each neighboring cell is depicted in yellow. (c) Color coding of canalicular network voxels depending on their nearest cell structure as a measure of the network area that is controlled by each cell. (d) Classification of canalicular junctions (nodes) according to the number of attached connections (degree). Red points depict interwoven nodes featuring a degree > 5. (e) Histogram (black) and cumulative plot (red) of the travel distance from canalicular voxels to the nearest cell through the network, showing that almost 70% of the canalicular network resides within a 10 µm travel distance. (f) The degree distribution of canalicular junctions is exponential (black line: fit ~ $\exp(-\beta d)$, $\beta = 0.87$) revealing the single-scale character of the canalicular network. There is a high

abundance of junctions with dendritic character (65 % of nodes show d = 3) but also junctions with up to 10 connecting canaliculi are present. The mean degree of nodes is 3.25. (g) The length distribution of individual canalicular structures is exponential (black line: fit ~ exp(-αl), $\alpha = 0.7\ \mu m^{-1}$) with individual lengths up to 15 µm. The mean canalicular length between two nodes is 2.15 µm. Scale bars are 20 µm.

Figure 3: Distance distribution between bone mineral and the osteocyte network. (a) z-Projection of the Euclidean distance of each mineralized matrix voxel to the closest cell voxel and (b) to the closest network voxel (either cell or canalicular structure). (c) Distance distributions show that 80% of the matrix voxels reside within a distance of 10 µm to the closest cell and (d) within only a distance of 1.4 µm to the closest canalicular network structure (the grey dashed line shows the distance from the closest cell for comparison). Due to the sample thickness of 20 µm, distance values above 10 µm (depicted with the dashed line in (c)) are not reliable and could be artifacts from the sample edges. Due to short mineral-cell network distances, these artifacts are not present in (d). Scale bars are 20 µm.

Figure 4: Osteocyte network and nanoscopic mineral particle properties. (a) Visualization of the osteocyte network showing highly organized (dense) osteocyte network structures at the top and the bottom and poorly organized (loose) network structures in the centre. (b) Synchrotron small angle x-ray scattering (SAXS) measurements of the mineral particle thickness (T-parameter) and (c) the mineral particle orientation (Rho parameter) along the visualized network structures. Mineral particles in dense network regions are thicker and more oriented as compared to the loose regions in the centre. The direction of alignment of mineral particles is always perpendicular to that of the canalicular structures. (d) Colocalization of T-parameter maps with the osteocyte network reveals thinner mineral particles around individual osteocyte lacunae. Scale bar 20 µm.

Figure 5: Correlation of microscopic network organization with nanoscopic mineral particle properties. (a) z-Projection of the Euclidian distance of mineralized matrix voxels to the osteocyte network structures. (b) Map of the according mineral particle thicknesses together with the

Accepted Article

osteocyte network organization. (c) Correlation of mineral particle thickness (T-parameter) with the distance of these mineral particles to the cell network. The T-parameter values shows a sharp mineral particle thickness distribution with an average of 2.75 ± 0.1 nm in dense network regions and broader distributions with an average T-parameter of 2.3 ± 0.3 nm in loose network regions. Color coding of histograms in (c) is consistent with the color code of the distance and T-parameter map in (a) and (b), respectively. Scale bar 20 μm.

Accepted Article

Accepted Article

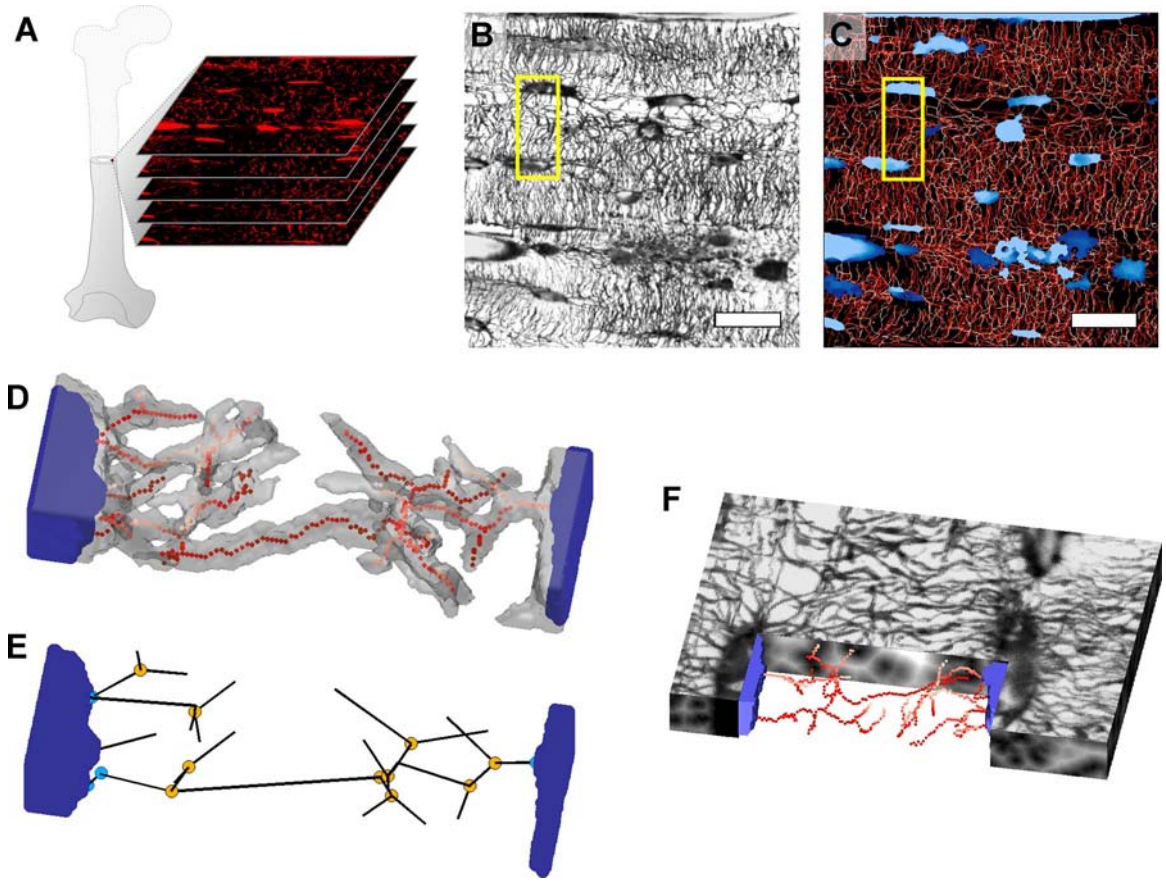

Figure 1

Accepted Article

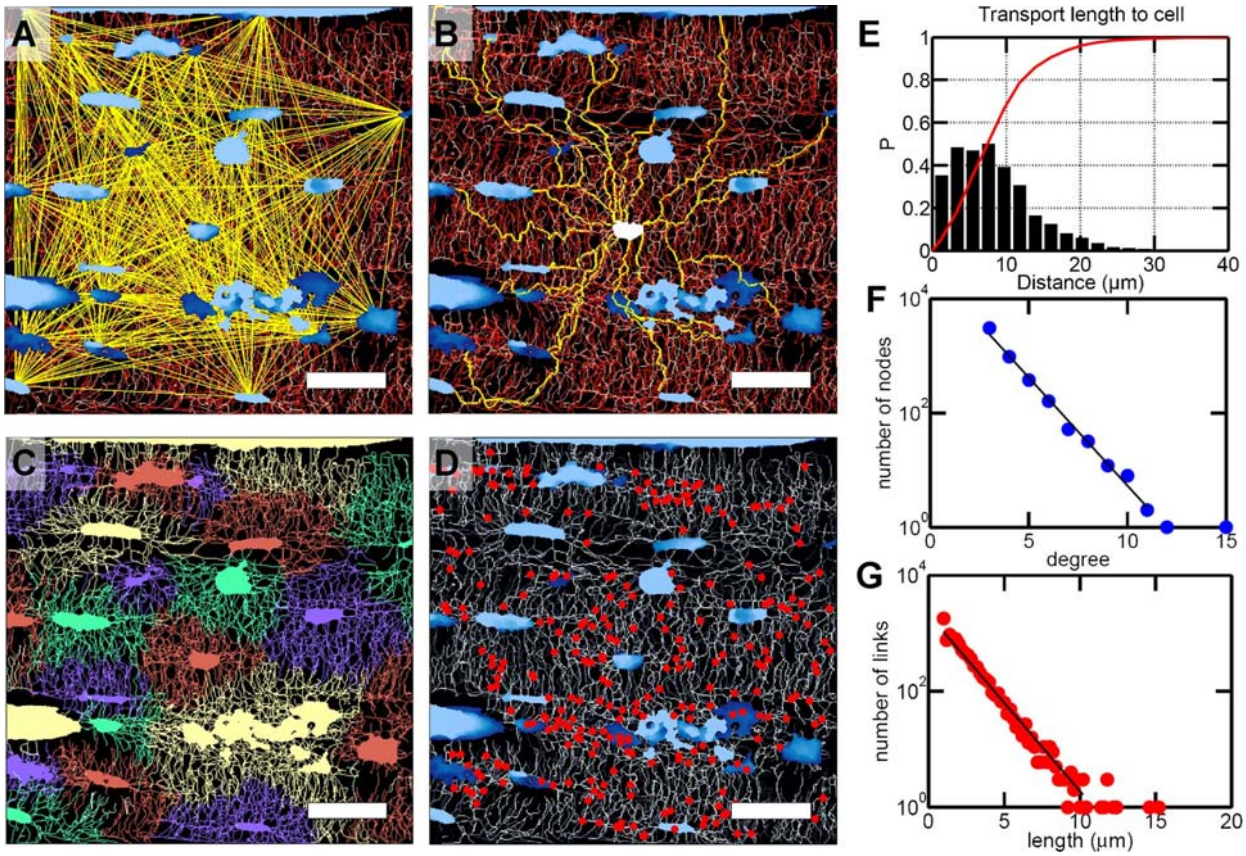

Figure 2

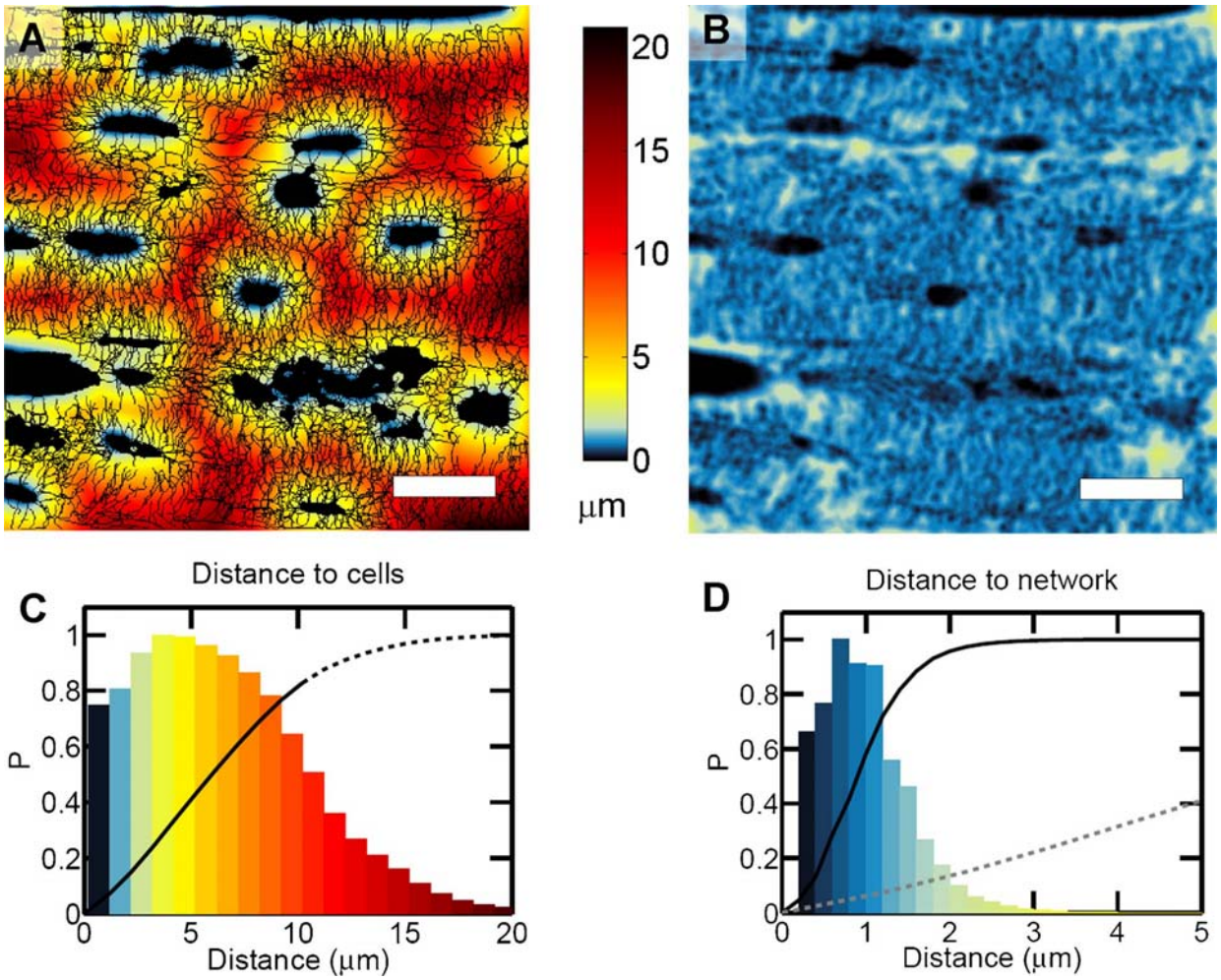

Figure 3

Accepted Article

Accepted Article

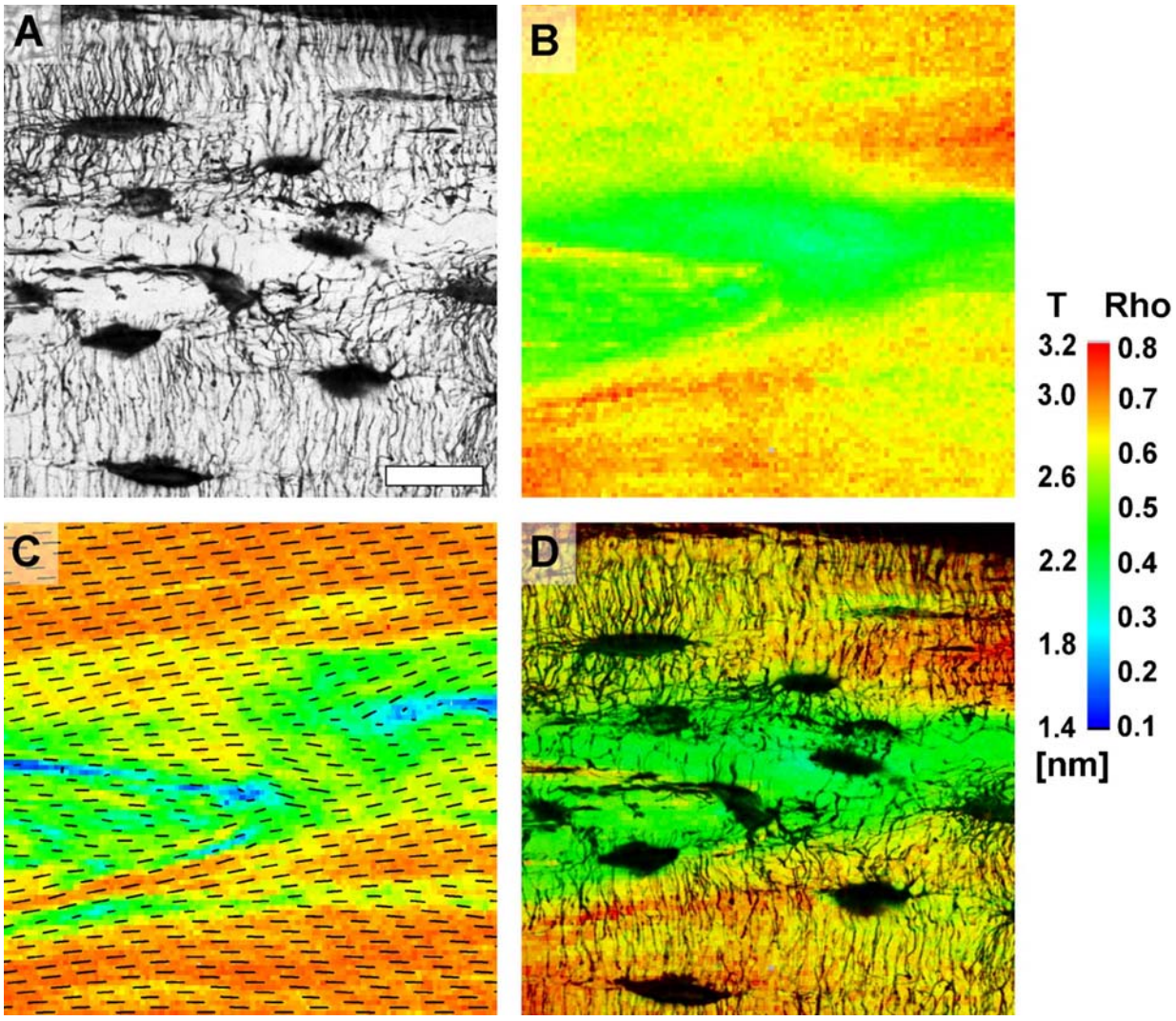

Figure 4

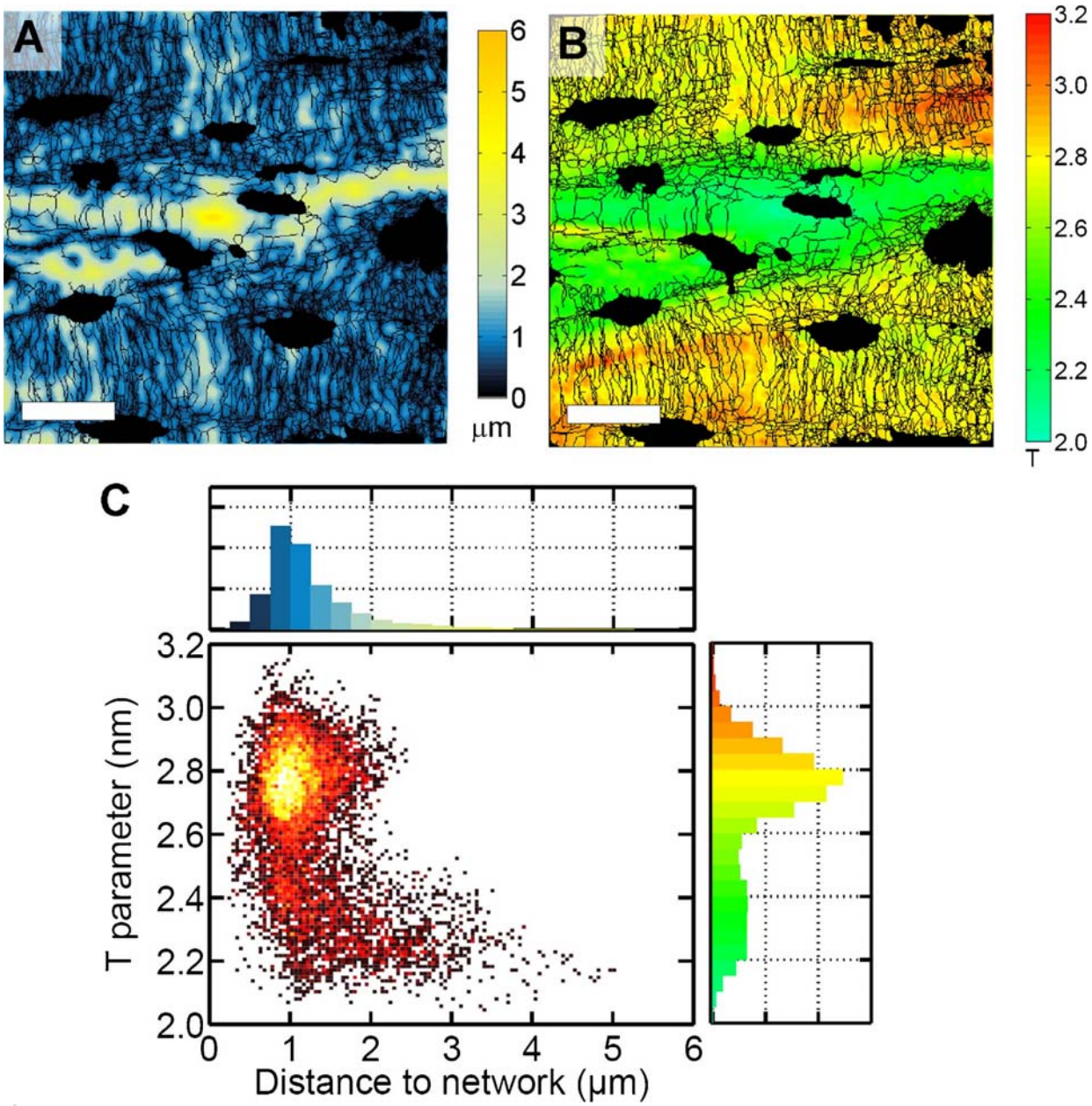

Figure 5

Accepted Article